ELSEVIER

Journal of Fluids and Structures 26 (2010) 406–429

JOURNAL OF FLUIDS AND STRUCTURES

www.elsevier.com/locate/jfs

Time-averaged topological flow patterns and their influence on vortex shedding of a square cylinder in crossflow at incidence

R.F. Huang[a,*], B.H. Lin[a], S.C. Yen[b]

[a]*Department of Mechanical Engineering, National Taiwan University of Science and Technology, Taipei, Taiwan 106, Republic of China*
[b]*Department of Mechanical and Mechatronic Engineering, National Taiwan Ocean University, Keelung, Taiwan 202, Republic of China*

Received 11 December 2008; accepted 7 January 2010
Available online 20 February 2010

Abstract

Flow characteristics around the square cylinder and their influence on the wake properties are studied. Time-averaged flow patterns on the surfaces of square cylinder in a cross-stream at incidence are experimentally probed by surface-oil flow technique and analyzed by flow topology for Reynolds numbers between 3.9×10^4 and 9.4×10^4 as the incidence angle changes from 0° to 45°. Vortex shedding characteristics are measured by a single-wire hot-wire anemometer for Reynolds numbers between 5×10^3 and 1.2×10^5. The effects of topological flow patterns on the wake properties then are revealed and discussed. Flows around the square cylinder are identified as three categories: the *subcritical*, *supercritical*, and *wedge* flows according to the prominently different features of the topological flow patterns. The Strouhal number of vortex shedding, turbulence in the wake, and wake width present drastically different behaviors in different characteristic flow regimes. A critical incidence angle of 15° separates the *subcritical* and *supercritical* regimes. At the critical incidence angle the wake width and shear-layer turbulence present minimum values. The minimum wake width appearing at the critical incidence angle, which leads to the maximum Strouhal number, is due to the reattachment of one of the separated boundary layer to the lateral face of the square cylinder. If the Strouhal numbers are calculated based on the wake width instead of the cross-stream projection width of cylinder, the data in the subcritical and supercritical regimes are well correlated into two groups, which would approach constants at high Reynolds numbers.

Keywords: Square-cylinder flow; Surface flow; Topological flow pattern; Vortex shedding

1. Introduction

Numerous studies have been carried out to investigate the aerodynamic characteristics of a bluff body which is used in fundamental and applied research in fluid dynamics. When a flow goes across a bluff body, e.g. a circular cylinder, a square cylinder, a wedge, or a sphere, complex flow phenomena and behaviors in the vicinity of the bluff-body surface and the wake region, e.g., flow separation, vortex shedding, shear-layer instability, etc., are usually induced.

*Corresponding author. Tel.: +886 2 2737 6488; fax: +886 2 2737 6460.
E-mail address: rfhuang@mail.ntust.edu.tw (R.F. Huang).

0889-9746/$ - see front matter © 2010 Elsevier Ltd. All rights reserved.
doi:10.1016/j.jfluidstructs.2010.01.003

Nomenclature

d	projected length of square cylinder on cross-stream direction
f_s	vortex shedding frequency in cylinder wake
Re_w	freestream Reynolds number based on w
St_d	Strouhal number of vortex shedding based on d
$St_{w'}$	Strouhal number of vortex shedding based on w'
T	turbulence intensity
T_{SL}	turbulence intensity in shear layers of cylinder wake
U	freestream velocity
u	local velocity in x direction
w	side width of square cylinder
w'	wake width at $x/w = 1$
x	Cartesian coordinate in axial direction
y	Cartesian coordinate in cross-stream direction
y_{SL}	location of shear layer in cross-stream direction
z	Cartesian coordinate along cylinder axis
x'	axial coordinate fixed at square cylinder
y'	cross-stream coordinate fixed at square cylinder
α	incidence angle
ρ	density of freestream fluid
Φ	power spectrum density function

For the case of a circular cylinder in crossflow, the curvature of the cylinder surface varies gradually with the downstream distance. The flow passing over the cylinder separates at some positions, which are drastically dependent on the Reynolds number. The phenomenon of transition from laminar to turbulent flow, which occurs in flow around the cylinder at certain values of the Reynolds number, should be taken into consideration due to its importance to the flow characteristics. However, for the case of a square cross-section cylinder in crossflow, the situation is quite different from the circular cylinder because the square cylinder has four sharp edges and the wall surface is flat between neighboring sharp edges. When the flow passes over the square cylinder, the separation points are fixed at the leading edges, the aerodynamics are said to be relatively insensitive to Reynolds number, but are more sensitive to the angle of incidence (Okajima, 1982). Consequently it is quite likely that the flow characteristics, aerodynamic forces, vortex shedding frequency, heat-transfer performance, etc., will exhibit distinct behaviors in different ranges of incidence angle of the square cylinder (Igarashi, 1984).

Most of the literature discussing the flow characteristics of the square cylinder in crossflow which was published during the past four decades was concerned with the pressure distributions, lift, drag, vortex shedding, as well as the instantaneous and averaged wake flow structures because of the increasing needs in wind engineering design, e.g., Vickery (1966), Bearman and Trueman (1972), Lee (1975), Rockwell (1977), Okajima (1982), Obasaju (1983), Norberg (1993), Tamura and Miyagi (1999), Luo et al. (2007), Tong et al. (2008), etc. Knisely (1990) reviewed the published Strouhal number data and summarized that the general tendency is of a rapid rise in the Strouhal number at relatively small angles of attack. He suggested that this rapid rise is associated with the reattachment of the separated shear layer. Other investigators, e.g. Saha et al. (2000), Dutta et al. (2003), and Sarioglu et al. (2005), reported similar trends for the behavior of the aerodynamic forces and vortex shedding.

Compared with the studies on the vortex shedding frequencies and aerodynamic forces mentioned in the above paragraphs, relatively few investigations which characterize the velocity field can be found in the literature. Durão et al. (1988), Lyn and Rodi (1994), Lyn et al. (1995), Ozgoren (2006), Hu et al. (2006), and Kurtulus et al. (2007) used laser Doppler velocimetry (LDV) or particle image velocimetry (PIV) to measure the time-averaged or instantaneous near-wake velocity field. Phase-averaged streamline patterns, time-averaged velocity profiles, and time-averaged turbulence properties in the near wake are illustrated for certain Reynolds numbers. However, details of the flow structure "near" the surfaces of the square cylinder are not shown because of the difficulties of measurements in this area. Igarashi (1984) used smoke and surface-oil flow visualization methods to study the characteristics of the flow around a square prism. He proposed that the flow patterns around the square cylinder can be classified into four regimes according to the range of the incidence angle, i.e., (I) $0^\circ \le \alpha \le 5^\circ$: perfect separation type with symmetric flow, (II) $5^\circ < \alpha \le 13^\circ$: perfect separation type with asymmetric flow, (III) $14^\circ \sim 15^\circ \le \alpha \le 35^\circ$: reattachment flow type, and (IV) $35^\circ < \alpha \le 45^\circ$: wedge flow type. van Oudheusden et al. (2005) reported the first successful measurements on the velocity field around the square cylinder. They used PIV to measure the velocity field around a square cylinder. Time-averaged flow patterns at $\alpha = 0^\circ$, 5°, 10°, and 15° were illustrated. At $\alpha = 0^\circ$ the boundary layers bifurcating from the stagnation point on the front face of the square cylinder separate readily from the leading edges of the side surfaces of the cylinder. Two large recirculation regions appeared in the wake behind the cylinder. Within the areas between the separated boundary layers and the side surfaces, recirculation regions were observed near the downstream portions of the side

surfaces of the cylinder. The flow structures near the upstream portions of the side surfaces, however, were unclear. With the increase of incidence angle, at the upper surface the side and rear recirculation regions gradually merged between $\alpha = 5^\circ$ and 10°, while at the lower surface the side recirculation was "pinched off" and mean flow reattachment occurred between $\alpha = 10^\circ$ and 15°. They noted that some unrealistic features occurring very close to the object, with streamlines crossing the cylinder surface, are the result of insufficient spatial resolution due to the chosen window size for the PIV image analysis, and therefore some of the near-surface flow structures as described above might not follow the rules of flow topology (Hunt et al., 1978). Some investigators, e.g., Taylor and Vezza (1999), Saha et al. (2000), Cheng et al. (2007), reported results of computational technique on the wake vortices and the unsteady flow around the square cylinder. However, detailed characteristics of the flow around the square cylinder still require further efforts.

As discussed in the above paragraphs, while the vortex shedding and aerodynamic forces of a square cylinder have been the subject of considerable research, less attention has been paid to the flow characteristics around the cylinder. Little information is available on the surface flow and its associated effects on the wake properties. Because the detailed flow characteristics around the cylinder are unclear, the physical mechanism leading to the existence of the critical incidence angle still remains an unsolved issue. The primary purpose of this study therefore is to investigate the characteristics of the flow around the square cylinder and discuss their effect on the vortex shedding properties. Because the collected data of the quantitative measurements are usually subject to blockage of camera view, low speed complex flow near the wall, etc., the measured results are ambiguous near the cylinder surfaces. This article cross-references the experimental results of the smoke-wire flow visualization and surface-oil flow and analyzes the characteristic flow patterns around the square cylinder by flow topology. The characteristic flow patterns are then used to discuss their influences on the vortex shedding in the wake.

2. Experimental arrangements

2.1. Test rig

The experiments were conducted in a closed-return wind tunnel. The wind tunnel had a test-section of $60 \times 60 \times 120\,\text{cm}^3$, made of one polished aluminum alloy plate as the floor and three high-transparency acrylic panels as the ceiling and side walls for photography and visualization. The contraction ratio of the nozzle was 10 to 1. The operating freestream velocity U in the test-section was adjustable between 0.3 and 60 m/s by an electronic inverter. The maximum turbulence intensity was less than 0.2% for $U > 3$ m/s. When the flow velocity was lower than about 3 m/s, the turbulence intensity gradually increased with the decrease of the freestream velocity. At $U = 0.5$ m/s the turbulence intensity increased to about 0.5%. The non-uniformity of the average velocity profile across the cross-section was smaller than 0.5%. For the surface-oil flow experiment, the average freestream velocity U was detected with a retractable Pitot tube along with a high precision electronic pressure transducer. The outer diameter of the Pitot tube was 3 mm. In order not to influence the flow field, the Pitot tube was retracted to the floor of the test-section when the flow investigation was carried out. The accuracy of the measurement of freestream velocity was affected primarily by the alignment of Pitot tube and the calibration of the pressure transducer. With the help of an on-line micro-pressure calibration system and the careful alignment of Pitot tube, the uncertainty of the freestream velocity measurement in the range of 9.75–23.5 m/s for the surface-oil flow experiment was estimated to be as large as 3% of the reading. For the wake instability experiment and the smoke-wire flow visualization, the freestream velocity was pushed lower than this velocity range. In order to avoid the increased inaccuracy induced by the viscous effect of using Pitot tube at low Reynolds numbers, a specially calibrated hot-wire anemometer was used to detect the freestream velocity at low speeds.

A hollow cylinder of square cross-section, as shown in Fig. 1(a), made of aluminum alloy (6061TET62) with a side width $w = 6$ cm and a span length $L = 60$ cm was used for the experiment. The aspect ratio L/w was 10. The geometric blockage ratio was 10–14% when α varies from 0° to 45°. According to West and Apelt (1982), the drag coefficient and Strouhal number of a cylinder with 10% blockage ratio at Reynolds number less than 10^5 may be increased by at most about 0.8% and 1.7%, respectively. Therefore, the effect of the blockage ratio in this study may not be significant. The influence of the aspect ratio requires more consideration. Stansby (1974), Fox and West (1990) and Gerich and Eckelmann (1982) discussed the effects of aspect ratio on the pressure force and vortex shedding of a circular cylinder. They proposed the use of cylinders with an aspect ratio greater than 30 or employment of end plates to the cylinder with a separation greater than 7 to reduce three-dimensional effects of the flow field. West and Apelt (1982) reported that the drag coefficient of the cylinder with an aspect ratio of 10 would present a value about 1.5% less than that with an aspect

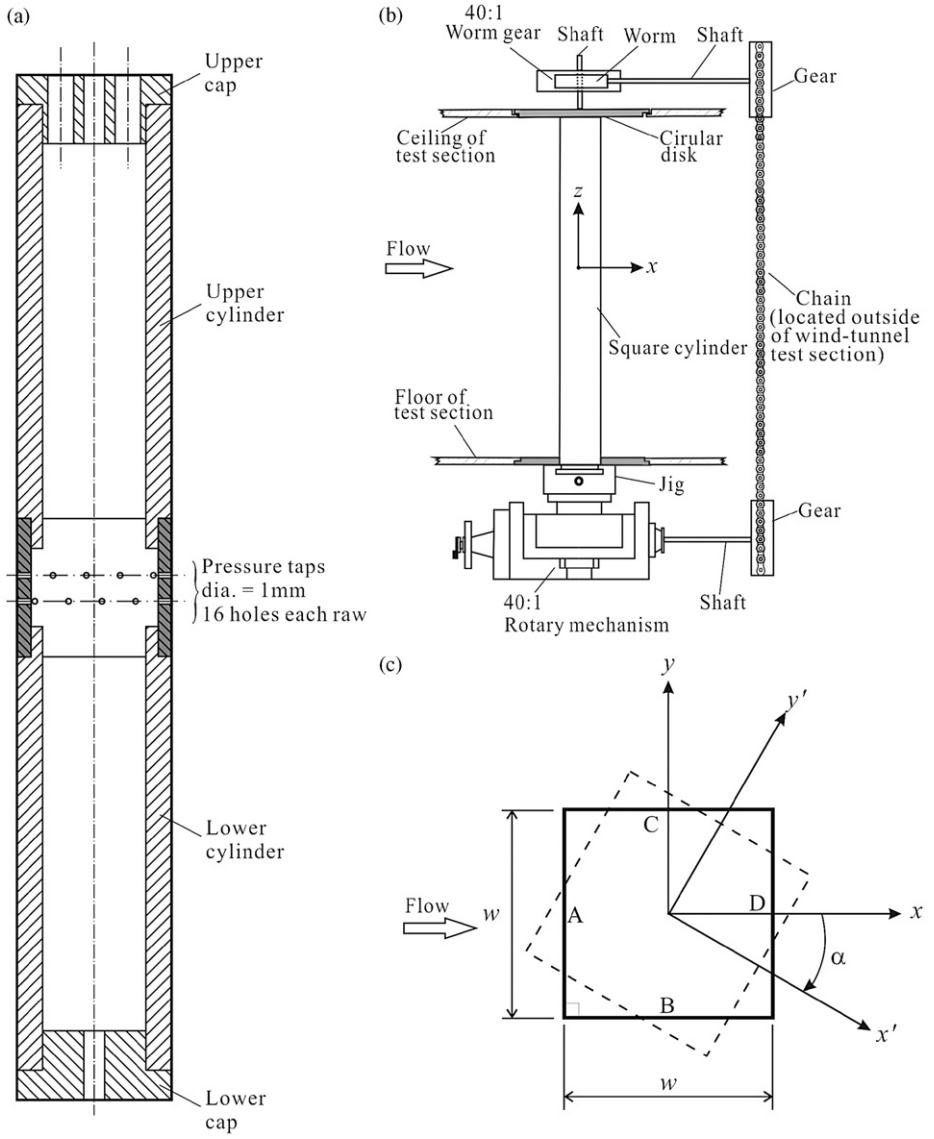

Fig. 1. Experimental set-up: (a) section view of square cylinder, (b) rotation mechanism and test rig, (c) definitions of coordinates, surfaces of cylinder, and incidence angle.

ratio of 40 at Reynolds numbers lower than 10^5. Szepessy and Bearman (1992) examined the effects of aspect ratio and end-plates on the vortex shedding and fluctuating lift. They found that the effect of changing aspect ratio is very strongly dependent on the Reynolds number. At Reynolds number 1.3×10^4, no difference of vortex shedding frequency was found between the cylinders with aspect ratios 1 and 11. At Reynolds number 4.5×10^4, about 5% decrease in Strouhal number might appear when the aspect ratio was decreased from 6.7 to 1. In this study, because end-plates were not installed for the cylinder of aspect ratio 10 operating at Reynolds numbers lower than 10^5, the flow field would inevitably be subject to the influence of three-dimensional effects. Therefore, observations on the flow patterns were made across the central section of cylinder for $z=\pm2w$ which was subject to less three-dimensional effects. Measurements of the vortex shedding and wake properties in this study were performed in the plane across the central section of the cylinder. The surface of the cylinder was carefully and slightly polished by using wetted magnesium-oxide particles of 0.2 μm. The cylinder was vertically installed in the wind tunnel test-section, as shown in

Fig. 1(b). It spanned from the floor all the way up to the ceiling of the wind tunnel test-section. The distance between the exit of the wind-tunnel nozzle and the front face of the square cylinder is 20 cm. The boundary layer thickness around this area is about 5 mm for freestream velocity $U = 30$ m/s, which was negligibly small when compared with the length of the square cylinder. The bottom end of the square cylinder was mounted on a precision rotary-mechanism. Circular disks were attached to the lower and upper ends of the square cylinder and sited on the floor and ceiling plates of the wind tunnel test-section. These circular disks were able to rotate with the rotation of the cylinder so that the flow in the test-section would not leak to the atmosphere. The rotary mechanism had a resolution of 0.0179°. It is worthy of note here that, after a tedious trial-and-error process during the experiments, it was found that the characteristic flow patterns were very sensitive to the incidence angle α of the square cylinder around the critical incidence angles α_{cri} and 45°. Therefore, the technique of setting the square cylinder to the target incidence angle became a very important factor for the identification of the flow pattern changes. The rotary mechanism was connected through a series of shaft, gear, chain, worm gear, and finally to the top of the square cylinder. In this way the square cylinder could be aligned stably and rotate smoothly. The operation range of the crossflow Reynolds number Re_w for the surface-oil flow experiment based on the cylinder width w was from 3.9×10^4 to 9.4×10^4 (corresponding to the freestream velocity U from 9.75 to 23.5 m/s). For wake instability detection, the lower limit of Reynolds number was 5×10^3 (corresponding to the freestream velocity 1.25 m/s).

The Cartesian coordinate system (x, y, z) was fixed to the mid-span and the center of the square cylinder, as shown in Figs. 1(b) and (c). The coordinates did not rotate with the rotation of the square cylinder. The freestream direction was always pointing to $+x$. The cross-stream and span directions were designated by y and z, respectively. Another coordinate system (x', y'), as shown in Fig. 1(c), was attached to the cylinder and could rotate with it. The incidence angle α was defined as zero when x' coincides with x. When the square cylinder rotates in the clockwise sense, the incidence angle α was designated as "positive". The four faces of the square cylinder were designated as A, B, C, and D. Face A was the front surface facing windward. Faces B and C were side faces. Face D was the rear surface facing leeward.

2.2. Smoke-wire flow visualization

The smoke-wire technique associated with high speed photography was firstly used to preliminarily visualize the "instantaneous" flow patterns at $Re_w = 20\,000$. The exposure time was 5 ms. Two corrugated Wolfram wires (i.e., the smoke wires) with 80 μm in diameter were installed in the mid-span plane. One was placed 20 mm upstream the leading edge of the square cylinder to make the forward flow observable. The other one was placed about 1 mm downstream the trailing edge to examine the reverse flows. By adjusting the density of corrugation, the thickness of the smoke streaks and the spacing between neighboring smoke streaks could be optimized. Thin mineral oil was brush-coated on the wire surface. The wire was ohmmically heated to generate fine smoke streaks. The surface temperature of the smoke-wire was maintained as low as possible, but still high enough to evaporate the oil, so that the upward convection velocity induced by buoyancy (Bejan, 1984) was lower than about 2 cm/s. The condensed vapor aerosols (the "smoke") of the thin mineral oil had diameters of about 1 ± 0.2 μm (Mueller, 1983). The slip factor and Stokes number (Flagan and Seinfeld, 1988) for these aerosols were estimated to be about 1.108 and 0.002, respectively, and therefore the smoke streaks were considered to be able to follow the flow properly.

2.3. Surface-oil flow visualization

The surface-oil flow pattern could display the time-averaged flow behaviors close to the surface (Squire, 1961). The surface oil-flow technique has been employed by many investigators to detect the characteristic flow patterns on the surface of a subject (e.g. Huang et al., 1996). They found that the locations of separation and reattachment of the boundary layer on the subject surface could be identified by examining the existence of the accumulated oil strips on the subject surface. Besides, by visually inspecting the flow directions of oil on the surface, the topological flow characteristics could be identified. In this study, mineral oil mixed with a small quantity of blue dye powder was blush-coated on the surface of the square cylinder. The flow direction on the cylinder surface was identified *in situ* from the trace of the oil flow motion and verified off-line from the recorded video movies. Dark traces on the cylinder surface were found where the massive dyed-oil accumulated. Positions of separation and reattachment of the boundary layer on the cylinder surface were identified from the recorded video images of the surface oil-flow patterns. According to the analysis of Squire (1961) and Merzkirch (1974), the uncertainty of identifying the position of characteristic points on the cylinder by using the surface-oil flow visualization method would be less than 8% at freestream velocity $U = 5$ m/s. The uncertainty decreased with increase of the freestream velocity.

2.4. Detection of wake instabilities and wake widths

The vortical instabilities in the cylinder wake were detected by a home-made, constant-temperature, one-component hot-wire anemometer. In order to detect properly the frequency of the vortical motions, the probe position was carefully adjusted in the y direction to capture the oscillation signals. Normally, the probe was placed at the position where the periodical signals revealed local maximum amplitudes. The output signals of the hot-wire anemometer were fed simultaneously to an FFT analyzer and a high-speed PC-based data acquisition system. During the experiment, the output signals of the hot-wire anemometer were monitored by using the FFT analyzer through the time and frequency domains to assure the appropriation of the probe position at all times. The data acquisition system had a sample-and-hold function for multi-channel acquisition without phase-lag. The hot wire probe used was TSI 1210-T1.5. The original tungsten wire was replaced by a platinum wire. The wire diameter and length were 5 μm and 1.5 mm, respectively. The dynamic response frequency corresponding to the electronic square-wave test was adjusted to 20 kHz. The sampling rate and the elapse time of the data acquisition system were set to 25 000 samples/s and 7 s, respectively. The accuracy for the hot-wire probe positioning was 10 μm. The accuracy of the shedding frequency detection depended not only on the response of hot-wire anemometer but also on the record length and sampling rate of the FFT analyzer. The uncertainty of the frequency detection was estimated to be within $\pm 0.75\%$ of the reading in this experiment.

3. Results and discussion

3.1. Smoke-streak flow patterns

Fig. 2 shows the "instantaneous" smoke flow patterns around and in the wake of the square cylinder. At $\alpha = 0^\circ$ and 7°, as shown in Figs. 2(a) and (b), the flows approach from the left to the right, form a stagnation point on face A, then bifurcate into two streams (going towards the edges of face A along the surface), finally separate from the front edges of faces B and C. The mirror-reflection images of the smoke streaks on face A are visible because the surfaces of the cylinder are polished. The stagnation point at $\alpha = 0^\circ$ is located at about the center of face A, while at $\alpha = 7^\circ$ it is displaced a little towards the lower part of face A. Vague traces of smoke can be observed within the areas between the separated boundary layers and the lateral surfaces of the square cylinder, particularly in the area near face B. Although it is difficult to distinguish the detailed flow structure in these areas, two sub-regions on face B filled with accumulated smoke which spread over the upstream and downstream portions, respectively, still can be identified. As the electric

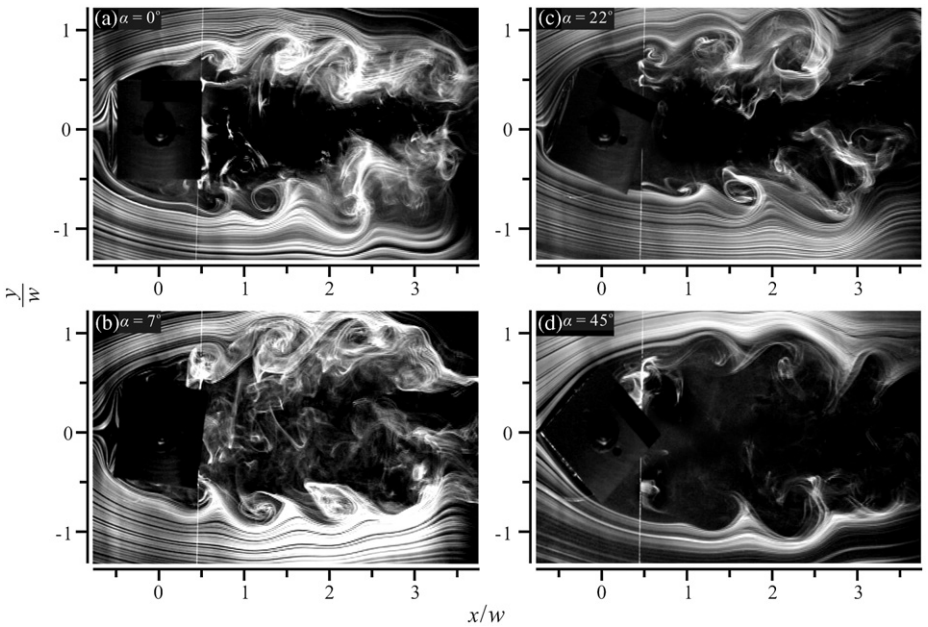

Fig. 2. Flow patterns obtained by smoke-wire flow visualization. $Re_w = 20\,000$. Incidence angle (a) $\alpha = 0^\circ$, (b) 7°, (c) 22°, (d) 45°.

power used to heat up the downstream smoke wire is shut down, the smoke present in these areas disappears. Therefore, the smoke which is visible in the regions between the separated boundary layers and the side surfaces of the square cylinder is carried by the reverse flow evolving from the wake region. Instability waves and shear-layer vortices appear along the separated boundary layers which have evolved from the front corners of the square cylinder. Movies of the video images show that the shear layers present unsteady up/down "flapping" motions with the evolution of vortex shedding in the wake, as discussed by Lyn and Rodi (1994) and Kareem and Cermak (1984). The "flapping" motions of shear layers are particularly obvious around the regions near the trailing corners of the square cylinder.

At $\alpha = 22^\circ$, as shown in Fig. 2(c), the stagnation point on face A shifts further downwards when compared with those in Figs. 2(a) and (b). The smoke streak separating from the leading edge of face B evolves to the downstream area. Part of the area between the separated smoke streaks and face B is obscured by the cylinder due to the perspective effect. The tilt-up angle of the smoke streak separating from the leading edge of face C is larger than those of Figs. 2(a) and (b). The detailed flow structures in-between the separated boundary layers and the side surfaces of the square cylinder are unclear because only few smoke particles are present near the rear edge of face C. Figs. 3(a) and (b) show the zoom-in images of the smoke streaks on faces B and C, respectively, at $\alpha = 22^\circ$. On face B (Fig. 3(a)), the smoke streaks separate from the leading edge, evolve a distance towards downstream area, and reattach to the surface. A recirculation bubble is formed on the portion near the leading edge of face B. The separated boundary layer observed in the recorded movie actually is unsteady. It sometimes separates from the corner between face A and face B and evolves downstream without reattachment. But most of the time it reattaches to face B to form the recirculation bubble as shown in Fig. 3(a). While on face C (Fig. 3(b)), the smoke streaks separate from the leading edge of face C and evolve to the downstream area at a large tilt-up angle without any reattachment to face C. The flow structure in-between the separated boundary layer and face C is unclear and requires further study.

At $\alpha = 45^\circ$, as shown in Fig. 2(d), the smoke streaks bifurcate at the leading edge of the square cylinder like a *wedge flow*. The bifurcated flows go along faces A and B without separation until they attain the rear edges. Careful and tedious experiments were performed to examine the flow patterns when the incidence angle was adjusted to be near 45°. It was found that, should the incidence angle not be adjusted exactly to 45° (say, a little smaller than 45°), the stagnation

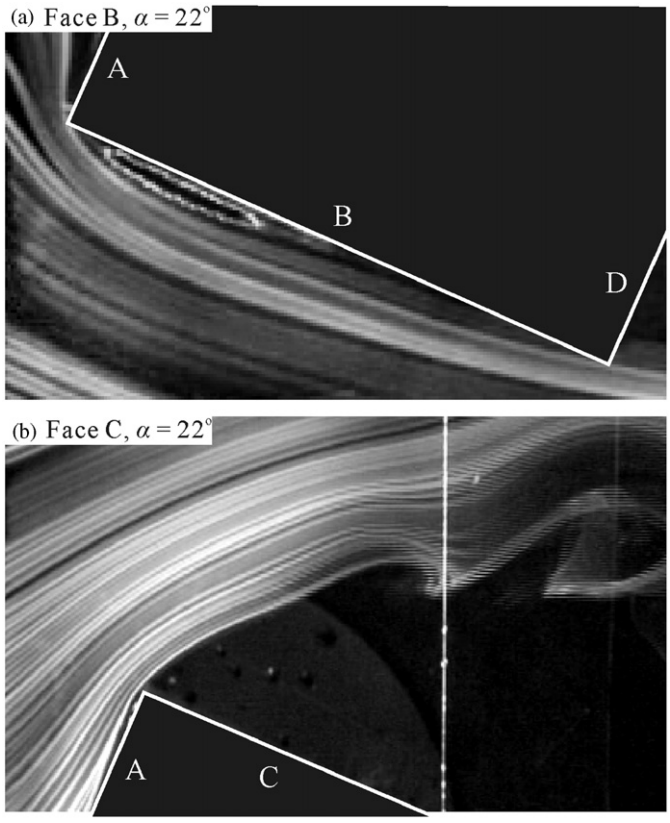

Fig. 3. Flow patterns obtained by smoke-wire flow visualization on (a) face B, (b) face C; $\alpha = 22^\circ$, $Re_w = 20\,000$.

point would always exist on face A at a location very near the junction between faces A and B. From the stagnation point on face A the flow bifurcates into two streams: one goes upward and the other goes downward along face A. The flow pattern on face B would present an unclear, small recirculation bubble located very near the leading edge of face B. When the incidence angle is adjusted exactly to 45°, the small recirculation bubble on face B disappears.

The detailed flow structures around the four surfaces of the square cylinder seem not to be satisfactorily revealed by the smoke-streak patterns. The surface-oil flow technique associated with the topological flow analysis, as stated in the following section, has therefore been adopted to examine the flows around the cylinder.

3.2. Surface flows and topological flow patterns

The topological flow analysis is employed to assist understanding of the time-averaged surface-oil flow patterns illustrated in this section. By virtue of Perry and Fairlie (1974) as well as Chong and Perry (1990), the topological flow pattern is characterized by *critical points*, *separatrices*, and *alleyways*. In the topological terminology, a critical point is a point in a flow field where the streamline slope is indeterminate, a separatrix is a streamline which leaves or terminates at a saddle, and an alleyway is a passageway in-between of two separatrices. By correctly describing the critical points, separatrices, and alleyways, the flow map can be clearly delineated. Hunt et al. (1978) have illustrated several characteristic critical points and separatrices like nodes, center, focus, saddle, bifurcation, etc. In the present case, the critical points consist of saddles and nodes. Topologically, the "center" and "focus" all belong to the category of "nodes". The "center" is located in a recirculation bubble for a two-dimensional flow, while the "focus" usually is the counterpart of the center as a three-dimensional phenomenon occurs. Because more or less three-dimensional effects were inevitably present in this study, as discussed in Section 2, the analyses of flow topology based on the surface-oil flow patterns observed around the mid-span section of the cylinder would contain features that imply the existence of these three-dimensional effects. Therefore, all the critical points of centers should be replaced by focuses for consideration of axial vortex stretching in the $\pm z$ direction induced by three-dimensional effects (Perry and Steiner, 1987). However, in order to make the flow features clearly delineated, two-dimensional topological flow patterns are presented in what follows.

3.2.1. Flow near face A

Fig. 4 shows the typical picture of the dyed oil flow on the middle section of face A. According to the observed results, the flow patterns in the range $-3.7 \le z/w \le 3.7$ are basically "almost two-dimensional" at all experimental

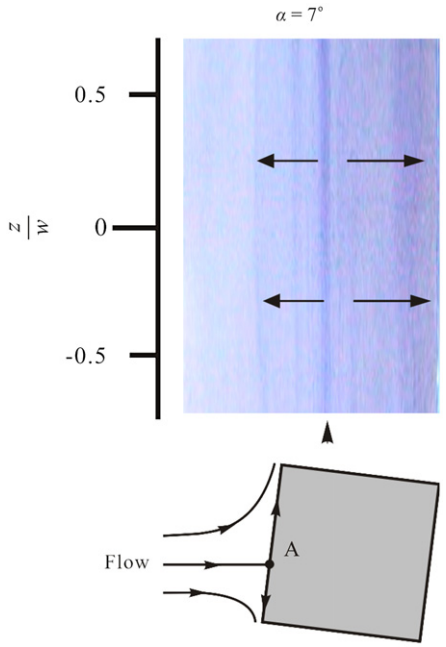

Fig. 4. Surface-oil flow pattern on face A; $\alpha = 7°$, $Re_w = 6.3 \times 10^4$.

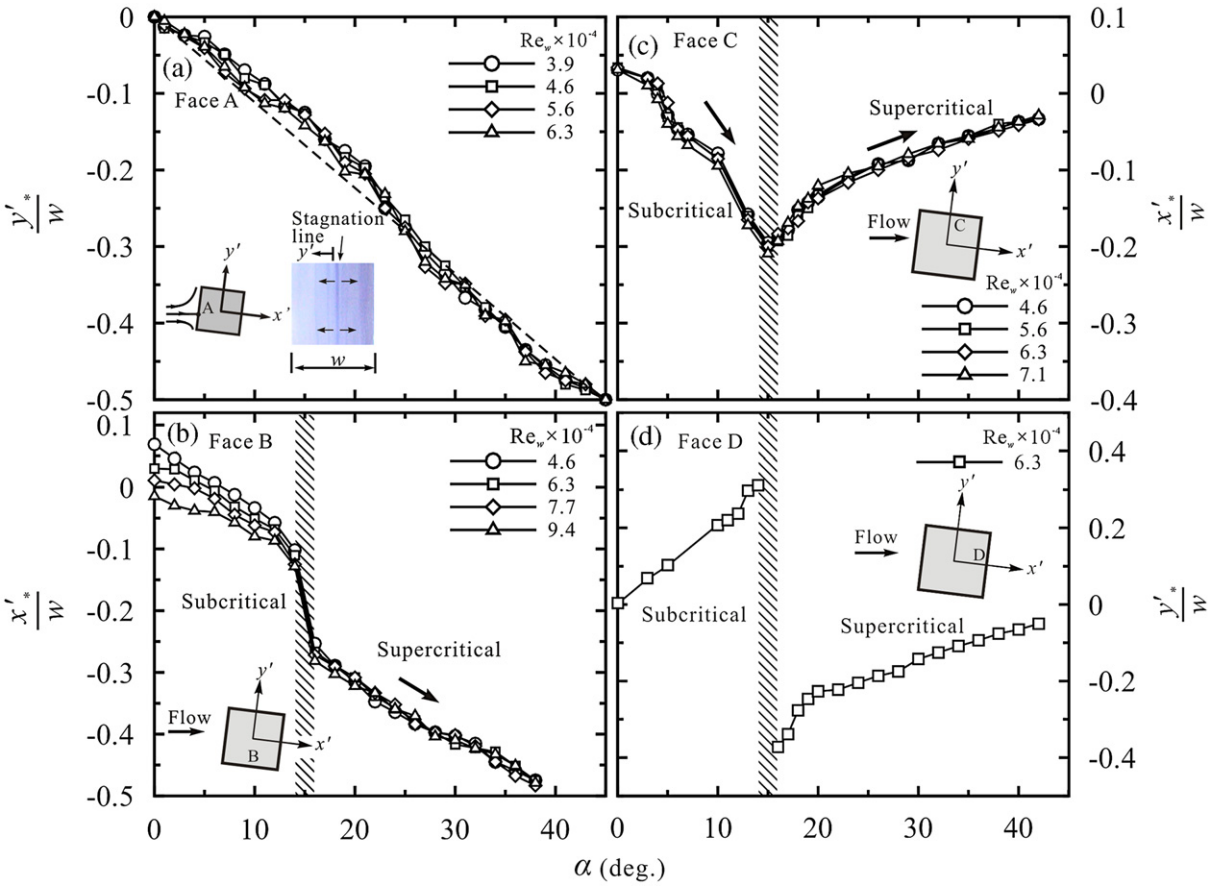

Fig. 5. Normalized locations of critical points on cylinder surfaces obtained by measuring surface-oil flow patterns.

incidence angles and Reynolds numbers. In Fig. 4 for $\alpha = 7^\circ$ and $\mathrm{Re}_w = 6.3 \times 10^4$, a narrow dark oil strip appears at $y'/w \approx -0.06$. The dark oil strip on the picture indicates the place where the dyed oil accumulates. The arrows marked on the picture delineate the visual directions of oil flow on the cylinder surface. Apparently, the free stream impinges on face A and bifurcates at the location of the dark oil strip because the flow directions on two sides of the dark oil strip point away from the strip. This scenario is shown by the hand sketch beneath the picture. The position of oil strip therefore is a stagnation point (a three-way saddle). All the flow patterns on face A at α smaller than 45° look similar to those in Fig. 4. The dark oil strip moves towards the junction between faces A and B with the increase of the incidence angle. At $\alpha = 45^\circ$, the oil strip disappears and all the oil flows on face A go towards the junction between faces A and C. During the experiment, a transparent scale, which is made of polynomial thin film of 15 μm in thickness, is attached to the cylinder surface to assist reading of the position of the dark oil strip. When measuring the positions of the dark oil strips, the images are magnified to about five times of the real scales and projected to the screen in order to reduce the measurement error. The normalized location y'_*/w of the stagnation point on face A at various incidence angles α and some selected Reynolds numbers Re_w are shown in Fig. 5(a). The Reynolds number does not appreciably affect the position of stagnation point. At $\alpha = 0^\circ$, the stagnation point is located at the center ($y'_*/w = 0$) of face A. The values of y'_*/w decrease with the increase of incidence angle in a slightly nonlinear fashion.

3.2.2. Flow near face B

Fig. 6 shows typical pictures of the dyed-oil flow on the middle section of face B at $\mathrm{Re}_w = 6.3 \times 10^4$. At $\alpha = 13^\circ$, as shown in Fig. 6(a), two dark oil strips appear. All the surface-oil flow patterns at $\alpha < 15^\circ$ present features similar to Fig. 6(a). At some incidence angles, the dark oil strips and the visual flow directions are a little difficult to distinguish, partially because of the low flow velocity existing there. In order to distinguish the ambiguous flow directions and oil strips, a special local flow visualization method is employed. A tiny quantity of $TiCl_4$ liquid droplet is introduced to the

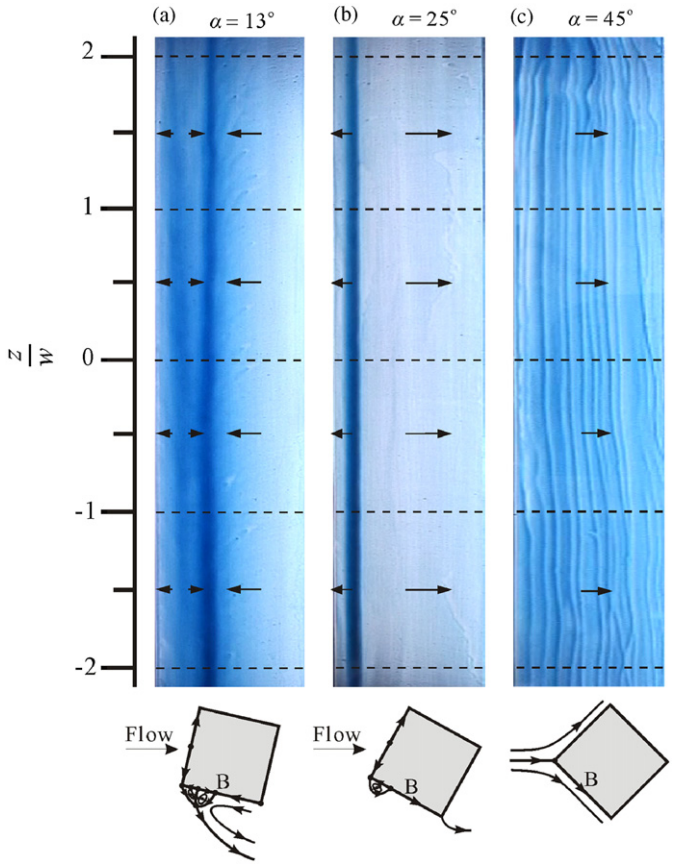

Fig. 6. Surface-oil flow pattern on face B at $Re_w = 6.3 \times 10^4$.

region where the dark oil strips and oil flow directions are ambiguous. By using a metal wire of 0.2 mm in diameter, the direction of the local flow becomes observable through the motion of white TiO_2 particles (the TiO_2 smoke particles are generated through the chemical reaction $TiCl_4+2H_2O \rightarrow TiO_2+4HCl$). It is found that the oil flows on two sides of the upstream dark oil strip (the left one) of Fig. 6(a) move away from the strip, while those on two sides of the downstream dark oil strip (the right one) move towards the strip, as indicated by the arrows shown in Fig. 6(a). Therefore, the flow which separates at the front edge of face B would form a complex flow structure in-between the separated boundary layer and face B. The flow above the upstream dark oil strip must go towards the strip to supply the surface flows on two sides of the strip (which are moving away from the strip), and therefore would form a "three-way saddle" there. However, the flow above the downstream dark oil strip must go out of the strip because the flows on two sides of the downstream strip move towards the strip, and therefore would form another "three-way saddle" there. The flow directions around the upstream three-way saddle are opposite to the corresponding directions around the downstream three-way saddle. By considering the flow topology, the scenario of the flow structure near the two three-way saddles is presented in the hand sketch beneath the picture of Fig. 6(a). The two black dots marked on face B denote the two dark oil strips in the picture. A dual-ring bubble with a vertex of four-way saddle must exist so that the separatrices and alleyways can satisfy the flow directions and the three-way saddles identified from the surface-oil flow pattern on face B. Downstream the downstream three-way saddle and near the wall, the flow must be reversed. As the reversed flow approaches the downstream three-way saddle, it must comply with the separatrix evolving from the downstream saddle and turns around towards the downstream area. The two-zone complex flow features near face B correspond to the smoke images with the two sub-region structure discussed in the previous section for Figs. 2(a) and (b). The surface-oil flow pattern with two dark oil strips (i.e., the dual-ring bubble) observed at $\alpha < 15^\circ$ is termed the "*subcritical mode*".

At $\alpha = 25^\circ$, as shown in Fig. 6(b), the surface-oil flow pattern looks drastically different from that of Fig. 6(a) – only a single dark oil strip appears. Flow patterns on face B observed in the range of $15^\circ < \alpha < 45^\circ$ are similar to Fig. 6(b). The flows on two sides of the single dark oil strip go away from the strip. Because the surface flow upstream the strip goes

upstream and the surface flow downstream the strip goes downstream, the dark strip is thus a three-way saddle with the flow above the strip going towards the strip. According to the observation on the smoke streak picture of Fig. 3(a), the single dark oil strip is a reattachment point of the separated boundary layer. In the hand sketch beneath the picture of Fig. 6(b), the black dot marked on face B denotes the dark oil strip (or the reattachment point) in the picture. A recirculation bubble must exist between the three-way saddle and the leading edge of face B, so that the separatrices and alleyways can satisfy the flow directions and the three-way saddles identified in the surface-oil flow pattern. The smoke-wire image shown in Fig. 3(a) is for unsteady flow at a low Reynolds number. "Unsteady" means that the separated shear layer evolving from the front edges of the square cylinder flaps: most of the time it reattaches to face B to form the recirculation bubble, but sometimes it separates. The surface-oil flow pattern shown in Fig. 6(b) is for a time-averaged surface flow pattern and at high Reynolds number. The directions of the oil-flow and the dark strip on face B suggest the time-averaged recirculation bubble length. The length of the unsteadily reattached recirculation bubble at low Reynolds number shown in Fig. 3(a) is instantaneous and thus is different from that of the time-averaged recirculation bubble at high Reynolds number shown in Fig. 6(b). Since the surface flow on face D near the downstream edge of face B goes towards the junction between faces B and D (this will be shown in Fig. 8), a separatrix evolving from the junction between faces B and D would go outwards from the junction and evolve towards the downstream area. The surface oil flow pattern with the single dark oil strip (i.e., the single recirculation bubble induced by the reattachment of separated boundary layer) observed in the range $15^\circ<\alpha<45^\circ$ is denoted as "*supercritical mode*". At $\alpha=45^\circ$, as shown in Fig. 6(c), no accumulated dark oil strip is observed and the surface-oil flow goes downstream without any reversal. This flow pattern corresponds to the "*wedge flow*" discussed in previous section for Fig. 2(d). The vertical traces of the oil streaks appearing in Fig. 6(c) may be induced by the shear effect of the attached boundary-layer flow or too much painting on the surface.

The normalized location x'_*/w of the "downstream oil strip" of the subcritical mode and the "single oil strip" of the supercritical mode on face B at various incidence angles α at some selected Reynolds numbers Re_w are shown in Fig. 5(b). In the *subcritical* range, the downstream strips at $\alpha=0^\circ$ are located at about the mid-position ($x'_*/w\approx 0$) of face B. The difficulty in the judgment of the unclear oil strip at small incidence angles makes the data scattered for different Reynolds numbers. The downstream oil strip moves upstream with the increase of the incidence angle. It attains $x'_*/w\approx -0.11$ at the incidence angle which is a little smaller than the critical value 15°. At $\alpha=15^\circ$, the surface oil flow pattern looks very obscure so that no data is presented. As the incidence angle is further increased to a value a little larger than the critical value of 15° the surface flow pattern changes to the supercritical mode (i.e., only one single dark oil strip appears on face B). Under this situation, the location of the reattachment point moves abruptly to $x'_*/w\approx -0.28$. As the incidence angle keeps increasing, the location of the single oil strip moves gradually towards the leading edge of face B. That is, the size of the reattachment-induced recirculation bubble in the supercritical range is much smaller than that of the dual-ring bubble in the subcritical range. The data for incidence angles larger than about 38° are not shown because the strips become somewhat blurred, and it is difficult to identify the exact positions. However, it is plausible to argue that the three-way saddle in the supercritical range may keep moving towards the upstream edge of face B with the increase of incidence angle, and finally disappear at $\alpha=45^\circ$ when the characteristic surface-oil flow pattern changes to the wedge flow mode.

3.2.3. Flow near face C

Fig. 7 shows the typical pictures of the dyed-oil flow on the middle section of face C at $\mathrm{Re}_w=6.3\times10^4$. The pictures present unclear images of oil patterns which look quite different from those of face B – no clear oil strips but oil bands appear. When the TiO_4 technique is applied to assist in the examination of the flow directions near the surface, it is found that the surface-oil flow directions behave similarly to those presented in Fig. 6. In Fig. 7(a) for $\alpha=5^\circ$, the oil flows on two sides of the upstream edge of the oil band go away from the upstream edge, while those on two sides of the downstream edge of the oil band go towards the downstream edge, as marked by the arrows in Fig. 7(a). All surface-oil flow pictures for $\alpha<15^\circ$ on face C present similar patterns to Fig. 7(a). By the same topological reasoning, the flow structure near face C, which is presented in the hand sketch beneath the picture of Fig. 7(a), should be similar to that in Fig. 6(a) for face B. The two black dots marked on face C denote respectively the up- and downstream edges of the oil band. A dual-ring bubble with a vertex of a four-way saddle must exist above the upstream three-way saddle. Downstream the downstream edge of the oil band, the flow must be reversed. In Fig. 7(b) for $\alpha=38^\circ$, the oil flows on two sides of the oil band go away from the band. With the help of the TiO_4 test, the bifurcation location, which is near the center of the band, can be identified. The surface-oil flow pictures for $15^\circ<\alpha<5^\circ$ have similar patterns to Fig. 7(b). At first glance, one may consider that the reattachment of the separated boundary layer will arise here. However, as has been demonstrated in Fig. 3(b), the smoke streaks separated from the front edge of face C show no reattachment (the separated smoke streaks shoot away from the leading edge of face C at a large angle and are subsequently curved to

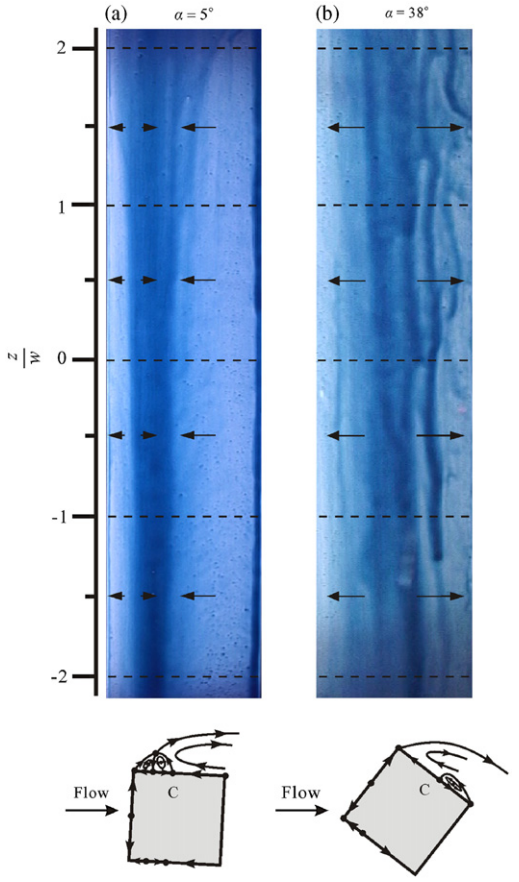

Fig. 7. Surface-oil flow pattern on face C at $Re_w = 6.3 \times 10^4$.

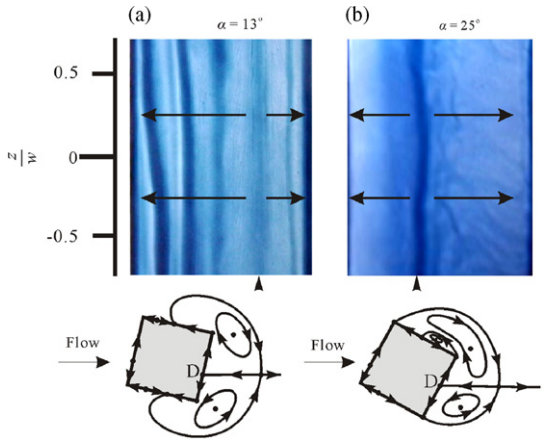

Fig. 8. Surface-oil flow pattern on face D at $Re_w = 6.3 \times 10^4$.

the downstream area); the flow structure on face C therefore would not behave similarly to the hand sketch of Fig. 6(b). Since the surface flows on both faces C and D near the junction between faces C and D go towards the junction (this will be shown in Fig. 8(b)), a separatrix evolving from the junction between faces C and D would go outwards from the junction. This separatrix leaving the junction between faces C and D would be deflected upstream by the reverse flow in the cylinder wake, reattach to face C, and form a recirculation bubble which covers the rear part of face C, as shown in

the hand sketch beneath Fig. 7(b). With this structure, the separatrices and alleyways can satisfy the flow directions and three-way saddle identified in the surface-oil flow pattern. At $\alpha = 45^\circ$, which is not shown here, the oil flow on face C goes all the way towards the junction between faces C and A. That is, the wide, shallow recirculation bubble existing in the rear part of face C in the *supercritical* range disappears at $\alpha = 45^\circ$. This fact can resemble the "bubble bust" phenomenon (Lissaman, 1983) observed on an airfoil. With the increase of the angle of attack, an aerodynamic wing at Reynolds numbers between 10^4 and 10^6 usually experiences a sequence of flow phenomena on its suction surface, such as attached flow, laminar separation, reattachment (which leads to a bubble appearing on the suction surface), and bubble burst (which is subsequently followed by a turbulent separation). The bubble appearing on the suction surface of the airfoil would exist within a range of angles of attack and disappear (burst) at the higher limit of this range. The bursting of the bubble always occurs in a discontinuous manner, resulting in a drastic change in the force coefficient.

The normalized locations x'_*/w of the downstream three-way saddle in the subcritical regime and the single three-way saddle in the supercritical regime at various incidence angles α and some selected Reynolds numbers Re_w, as shown in Fig. 5(c), behave differently from those shown in Fig. 5(b) for face B. In the subcritical range the downstream strip on face C at $\alpha = 0^\circ$ is located at $x'_*/w \approx 0.03$, which is a little downstream of the middle of face C. It moves upstream as the incidence angle is increased and reaches $x'_*/w \approx -0.2$ at an incidence angle of about 15°. As the flow pattern changes to the supercritical mode in the range of $15^\circ < \alpha < 45^\circ$, the single dark oil strip does not move further upstream like that presented in Fig. 5(b). Instead, it moves towards the center of face C as the incidence angle is increased. The positions of the three-way saddles on faces B and C in the supercritical regime show different behaviors because the flow structures on these two faces are different – on face B it is a leading-edge recirculation bubble induced by reattachment of the separated boundary layer, while on face C it is a wide, shallow recirculation bubble covering the rear part of face C. The leading-edge bubble on face B shrinks in size with the increase of the incidence angle, while the three-way saddle on face C moves gradually towards the center of face C with the increase of α.

3.2.4. Flow near face D

The typical surface-oil flow patterns on face *D* (i.e., the rear face) are shown in Fig. 8. When the incidence angle is smaller than 45° the single dark oil strip pattern as typically shown in Figs. 8(a) and (b) is always observed in either the subcritical or the supercritical regime. The single oil strip in the subcritical regime is always located in the right portion of face D. While the single oil strip in the supercritical regime is always located in the left portion of face *D*. The oil flows on two sides of the dark oil strip go away from the strip. Apparently, the single dark oil strip appearing on face *D* is a three-way saddle. The flow above the strip goes towards it. In order to comply with the flow directions and the three-way saddles identified from the surface-oil flow pattern, a large recirculation bubble with a four-way saddle existing at a position far from face D in the wake region is proposed in the hand sketches beneath Figs. 8(a) and (b). The single oil strip in the supercritical regime moves towards the center of face D with the increase of α as $\alpha < 45^\circ$. At $\alpha = 45^\circ$, the characteristic flow pattern changes: although not shown here, the oil strip disappears and the oil flow on face *D* goes towards the junction between faces *D* and *B*. This change is very sensitive to the incidence angle. During experiment, if the incidence angle is adjusted close to 45° but not exactly at 45°, the single oil strip pattern would appear near the centers of faces D and C.

The normalized location y'_*/w of the three-way saddle on face *D* at various incidence angles α and Reynolds numbers Re_w are shown in Fig. 5(d). At $\alpha = 0^\circ$, the dark oil strip is located at the center of face D. In the subcritical regime the normalized location of the dark oil strip moves from $y'_*/w = 0$ at $\alpha = 0^\circ$ towards the junction between faces C and D and attains $y'_*/w \approx 0.31$ as α approaches the critical incidence angle of 15°. As the incidence angle just passes the critical value, the dark oil strip shifts drastically from $y'_*/w \approx 0.31$ to $y'_*/w \approx -0.38$. Continuing to increase the incidence angle in the supercritical range would make the dark oil strip move towards the center of face D. The data of y'_*/w for α greater than about 42° are not shown in Fig. 5(d) because the images of the oil strip become blurred and difficult to identify in that region. However, it is clear that the stagnation point induced by the reverse flow of the wake bubble would appear at the junction between faces C and D at $\alpha = 45^\circ$.

3.2.5. Topological flow patterns

According to the results and analyses of flow visualizations discussed in the above sections, the two-dimensional topological flow patterns of the *subcritical*, *supercritical*, and *wedge* flow modes around the square cylinder are proposed in Figs. 9(a), (b) and (c), respectively. The patterns represent time-averaged flow characteristics because they are obtained from the surface-oil flow patterns, instead of the instantaneous smoke streak flow patterns.

As shown in Fig. 9(a) for the *subcritical* mode, a forward stagnation point (S'_1), which is a three-way saddle, appears on face A. The bifurcated flows on face A separate at the two front corners and form two three-way saddles S'_2 and S'_5. Near the upstream part of faces B and C, the dual-ring bubbles are characterized by several three-way saddles (S'_3 and S'_4

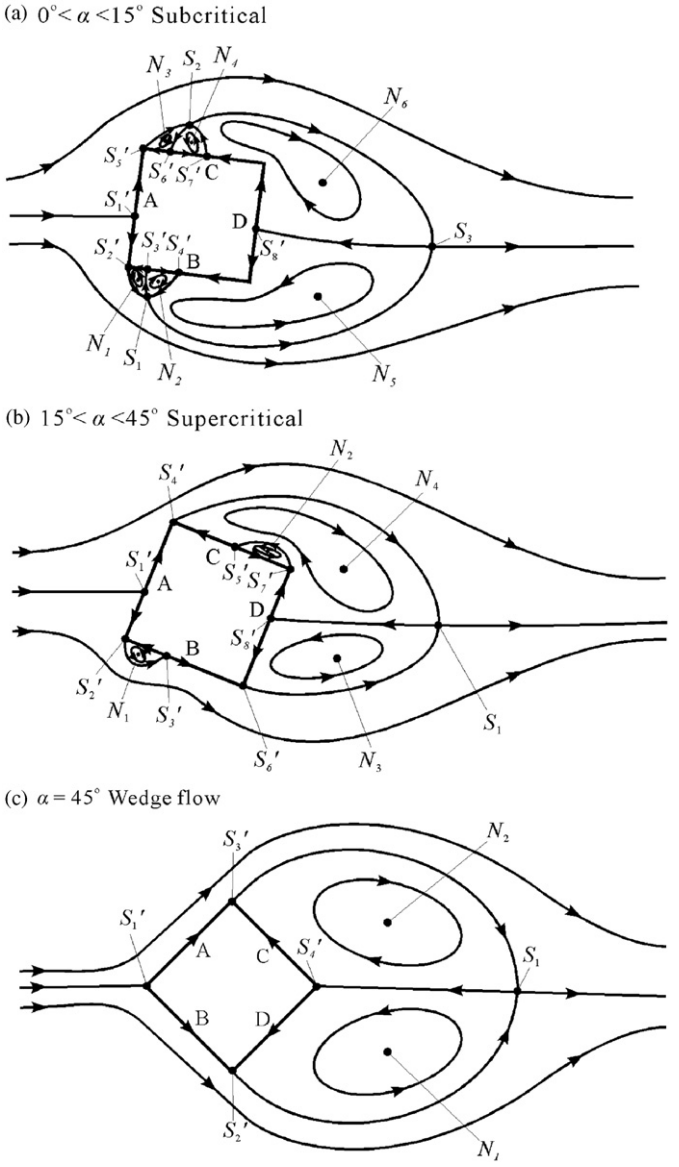

Fig. 9. Two-dimensional topological flow patterns around square cylinder.

on face B and S_6' and S_7' on face C), four-way saddles (S_1 above face B and S_2 above face C), and nodes (N_1 and N_2 centering at dual-ring bubble above face B and N_3 and N_4 centering at dual-ring bubble above face C). The dual-ring bubble is composed of two counter-rotating vortices. The three-way saddles S_3' and S_4' on face B denote the upstream and downstream oil strips shown in Fig. 6(a), respectively. While the saddles S_6' and S_7' on face C denote the upstream edge and downstream edge of the oil band shown in Fig. 7(a), respectively. An aft stagnation point S_8' on face D and a four-way saddle S_3 in the near wake region construct a large near-wake bubble. The large bubble located downstream face D is composed of two large counter-rotating vortices which are centered at the nodes N_5 and N_6. This recirculation bubble looks similar to those usually found in a bluff-body wake. Because the surface flows on the downstream portions of both faces B and C go in the upstream direction (as has been shown in Figs. 6(a) and 7(a)), the flows near the rear parts of faces B and C respectively must go reversely, and make turns to comply with the separatrices evolving from the vertex points of the dual-ring vortices existing near the upstream parts of faces B and C. Hunt et al. (1978) obtained a general formula for the relationship between the number of nodes (including four-way nodes N and three-way nodes N')

and saddles (including four-way saddles S and three-way saddles S') for the flow around the surface obstacles. The topological rule is

$$\left(\Sigma N+\tfrac{1}{2}\Sigma N'\right)-\left(\Sigma S+\tfrac{1}{2}\Sigma S'\right)=1-n,$$

in which n is the connectivity of the section of the flow under consideration. In this case, $n=2$ because one solid obstacle is present in the flow field. By counting the number of critical points in Fig. 9(a), it is obvious that the proposed flow pattern satisfies the topological rule

$$\left(\Sigma N+\tfrac{1}{2}\Sigma N'\right)-\left(\Sigma S+\tfrac{1}{2}\Sigma S'\right)=-1.$$

The proposed two-dimensional model of subcritical mode shown in Fig. 9(a) has little difference from the results of PIV measurements (for $\alpha<15^\circ$) of van Oudheusden et al. (2005). This may be induced by the three-dimensional effect. Although end-plates were installed on a square cylinder with an aspect ratio of 11.7 in the Oudheusden et al. work, more or less three-dimensional effects may still arise. Three types of three-dimensional topological flow patterns for subcritical models are proposed in Fig. 10 to fit Oudheusden et al.'s measurements. All three types of flow patterns on face A and the upstream portions of faces B and C shown in Fig. 10 are the same as those shown in Fig. 9(a). The flow structures near the downstream portions of faces B and C and the near-wake regions, however, are slightly different among the three types. An aft stagnation point S_8' on face D and a four-way saddle (S_5 for type I, S_4 for type II, S_3 for type III) in the near-wake region construct a large near-wake bubble. The large bubble downstream face D is composed of two large counter-rotating vortices which are centered at the nodes N_7 and N_8 for type I, N_6 and N_7 for type II, and N_5 and N_6 for type III. Because the surface flows on the downstream portions of faces B and C go towards the upstream direction, as has been shown in Figs. 6(a) and 7(a), the topological flow structure around these regions may display slightly different appearance, as shown by types I, II, and III of Fig. 10. For type I, two four-way saddles S_3 and S_4 exist near the rear corners of the square cylinder so as to form two small vortices on the downstream portions of faces B and C. For type II, the four-way saddle near the junction between faces C and D disappears, and thus the reverse flow of the clockwise-rotating vortex of the near-wake recirculation bubble extends to the downstream portion of face C. For type III, both the four-way saddles near the rear corners of the square cylinder disappear and the reverse flow of the large near-wake recirculation bubble reaches upstream, and then attains the downstream portions of faces B and C. The near-wake flow patters shown in types I, II, and III of Fig. 10 resemble the PIV results obtained by van Oudheusden et al. at $\alpha=0^\circ$ and 5°, 10°, and 15°, respectively. However, the dual-ring bubbles appearing on the upstream portions of faces B and C are not shown in the van Oudheusden et al. work because of the resolution limitation of PIV.

As shown in Fig. 9(b) for the *supercritical* mode, different flow patterns on faces B and C are proposed according to the observations and analyses of Figs. 6(b) and 7(b) in the previous sections. On face B, a recirculation bubble with a reattachment point S_3' appears on the upstream portion of face B because the reattachment of the separated boundary layer evolves from the three-way saddle S_2'. Since both the surface flows on the downstream portions of faces B and C in the *supercritical* regime go in the downstream direction, and the surface flow on face D branches off towards the rear corners of the cylinder, three-way saddles S_6' and S_7' must exist at the rear corners. Because the surface flow on the downstream portion of face B goes downstream, the separatrix evolving from the three-way saddle S_6' would not go reversely towards the upstream area. However, the situation near face C is different since the separated boundary layer evolving from the leading edge of face C does not reattach to face C, as has been shown in Fig. 3(b). Since the surface flows on the rear and front parts of face C bifurcate at the three-way saddle S_5', the separatrix evolving from the three-way saddle S_7' would move towards the upstream direction and reattach to the three-way saddle S_5'. A wide, shallow recirculation bubble would therefore be formed around the center N_2. The reverse flow of the wake vortex would cover the wide, shallow vortex on rear part of face C, attain the leading edge of face C, and make a turn to comply with the separated shear layer evolving from the leading edge of face C. The difference between the flow structures above faces B and C makes the large wake vortex (which is vertexed at the four-way saddle S_1) drastically asymmetric.

The proposed topological flow pattern for the *wedge* flow mode appearing at $\alpha=45^\circ$ is shown in Fig. 9(c). Since the surface flow on each of the four faces of the square cylinder is unidirectional, no three-way saddles will exist on each face. The leading edge recirculation bubble centering at N_1 on face B and the trailing edge recirculation bubble centering at N_2 on face C of the supercritical mode (Fig. 9(b)) disappear. The free stream impinges the cylinder at the nose point and forms the three-way saddle S_1'. On faces A and B the boundary layers are attached to the surfaces. Because the surface flows on faces A and C merge at the junction between faces A and C, a three-way saddle S_3' is formed. The same situation happens on face B and the three-way saddle S_2' can be found at the junction between faces B and D. The separatrices evolving from S_3' and S_2' go downstream and enclose the large near-wake recirculation bubble which is characterized by the three-way saddle S_4', the four-way saddle S_1, and the nodes N_1 and N_2.

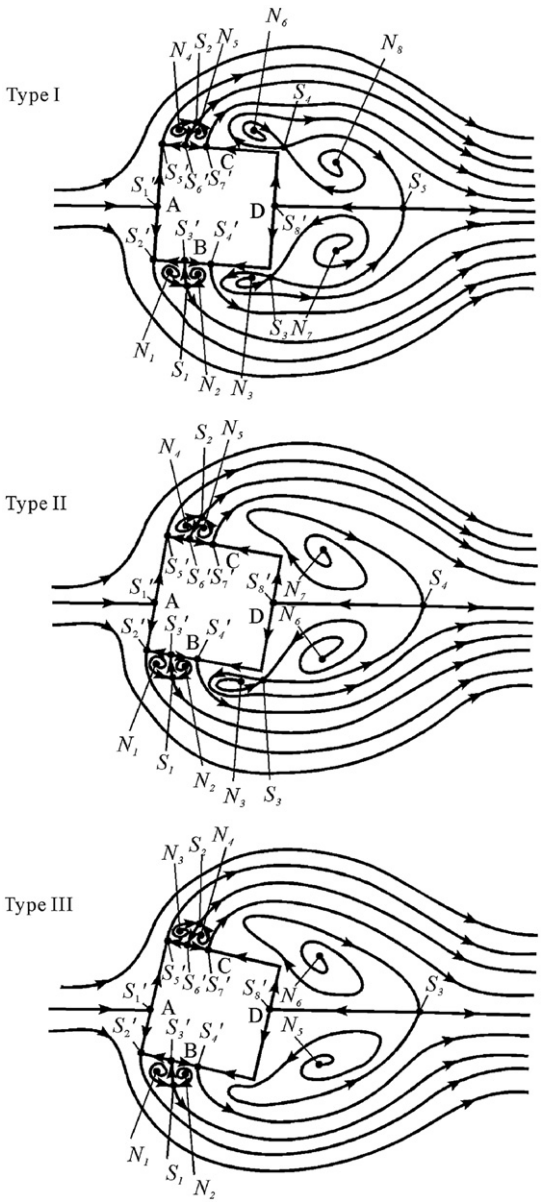

Fig. 10. Topological flow patterns around square cylinder with three-dimensional effects in *subcritical* regime ($0^\circ \le \alpha < 15^\circ$). For type I to III in the *subcritical* regime, the angle of incidence is slightly increasing. Type I exists at α smaller than about 5°, type III exists at α larger than about 10°, and type II appears for α between about 5° and 10°.

3.3. Vortex shedding and wake width

Fig. 11(a) shows the time series of the typical velocity signals detected in the near wake by applying a single-wire probe of the hot-wire annemometer at $Re_w = 6.3 \times 10^4$. The measurement position is $(x/w, y/w, z/w) = (4, -0.5, 0)$. Traverses in the spanwise direction indicated no substantial dependence of the vortex shedding frequency on z in the range of $-3.7 < z/w < 3.7$. In Fig. 11(a), typical vortex shedding signals in time domain in the wake are shown: periodic signals are superimposed with fluctuations. It is converted to frequency domain as a power spectrum density function by using the fast Fourier transform (FFT) technique, as shown in Fig. 11(b). The vortex shedding frequency f_s corresponding to the time series of Fig. 11(a) is 42.7 Hz, as indicated by the peak value of Fig. 11(b). Fig. 11(c) shows the frequency distributions of the vortex shedding, which are obtained from the power spectrum density functions for

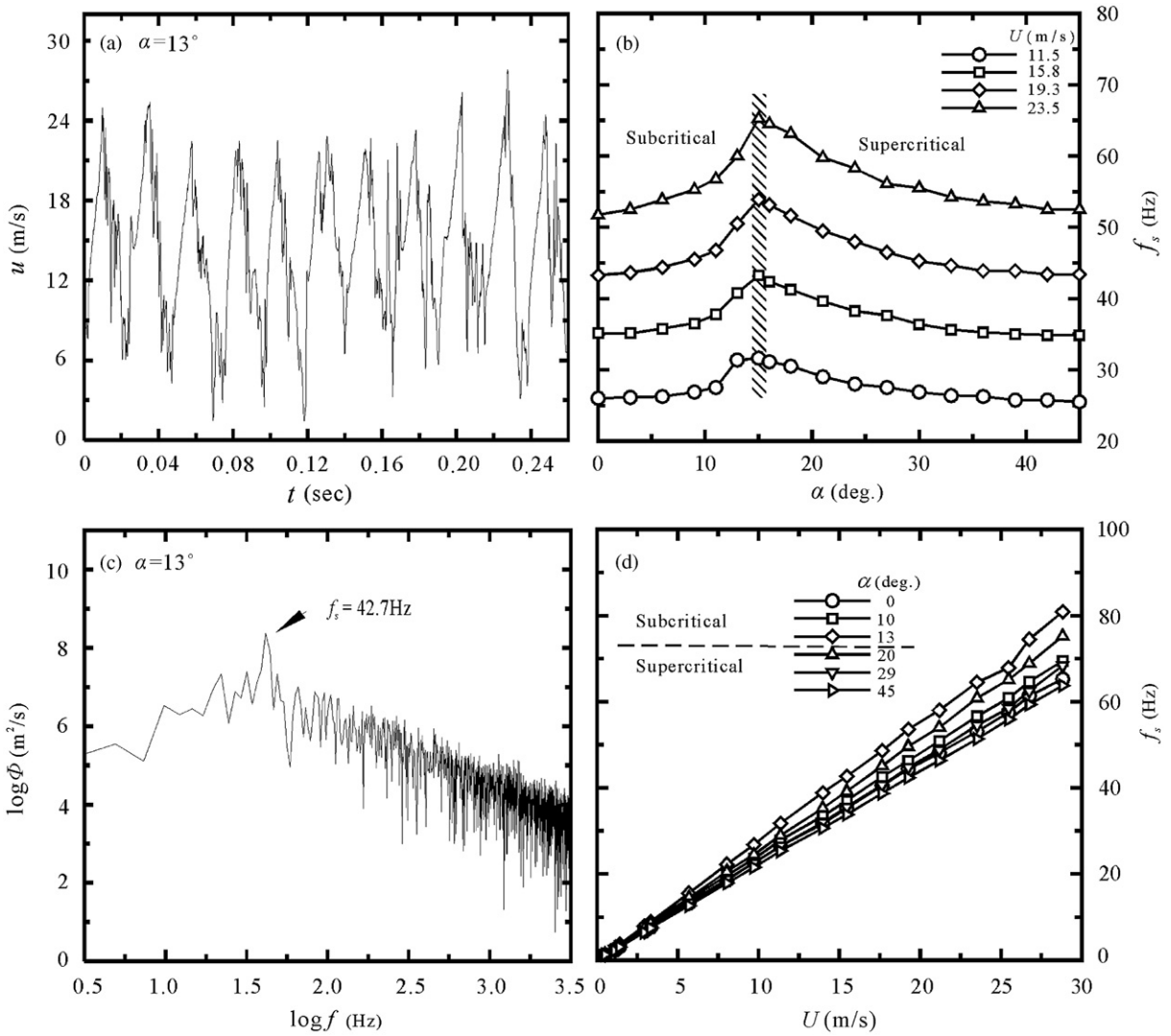

Fig. 11. Data measured by hot-wire anemometer in cylinder wake at $(x/w, y/w, z/w) = (4, -0.5, 0)$: (a) instantaneous axial velocity, $\alpha = 13^\circ$, $Re_w = 6.3 \times 10^4$, (b) power spectrum density function, $\alpha = 13^\circ$, $Re_w = 6.3 \times 10^4$, (c) variation of vortex shedding frequency with incidence angle, (d) variation of vortex shedding frequency with freestream velocity.

$0^\circ \le \alpha \le 45^\circ$ at various freestream velocities U. It is apparent that for each specific freestream velocity U, the vortex shedding frequency increases with increasing incidence angle from a low value at $\alpha = 0^\circ$ to a peak value at $\alpha = 15^\circ$, then decreases to a value almost identical with that for $\alpha = 0^\circ$ and $\alpha = 45^\circ$. For instance, f_s has almost the same value of 35 Hz at $U = 15.8$ m/s ($Re_w = 6.3 \times 10^4$) for both $\alpha = 0^\circ$ and 45°. The incidence angle for the peak frequencies coincides with the critical α for the characteristic flow modes. For a specific incidence angle, the vortex shedding frequency increases linearly with the increase of freestream velocity, no matter if it is in the *subcritical* or *supercritical* regime, as shown in Fig. 11(d).

The raw frequency data shown in Fig. 11 are converted to a Strouhal number St_d based on the width of the cylinder projection on the cross-stream plane (the y-z plane), d, which is calculated according to the formula

$$d/w = \sqrt{2}\sin(45^\circ + \alpha).$$

The Strouhal number defined by $St_d \equiv fd/U$ is frequently used to correlate the dynamic data in the wake (Strouhal, 1878). The reason why the projection width d is used as the length scale for Strouhal number instead of the cylinder width w is due to the

conventional usage for non-circular objects, for instance a flat plate, airfoil, elliptic oval, wedge, etc. By using the projection width for Strouhal number, investigators usually can obtain satisfactory correlation results between the Strouhal number and the Reynolds number except in the viscosity dominated regime. This is because the Strouhal number is a non-dimensional group in which the viscous effect is not taken into account. It represents only the inertial effect on the instability frequency. Applying similarity theory and dimensional analysis to the inertial and unsteady terms in the Navier Stokes equations, it can be found that the Strouhal number would approach a constant in the inertia-dominated range (Huang and Lee, 2000). For example, Roshko (1955) found that the Strouhal number based on the cross-stream length scale remains nearly constant at 0.21, 0.18, and 0.14 for a circular cylinder, 90° wedge, and flat plate, respectively, at Reynolds numbers between 10^3 and 10^5. This indicates that a blockage body with shaper edges would lead to a smaller Strouhal number. The correlations between the Strouhal number and the incidence angle as well as the Strouhal number and the Reynolds number are shown in Figs. 12(a) and (b), respectively. In Fig. 12(a), the Strouhal number for a specific Reynolds number, for instance, $Re_w = 6.3 \times 10^4$, increases with increasing incidence angle from about 0.133 at $\alpha = 0°$ to a maximum about 0.2 at $\alpha = 15°$, then decreases a little

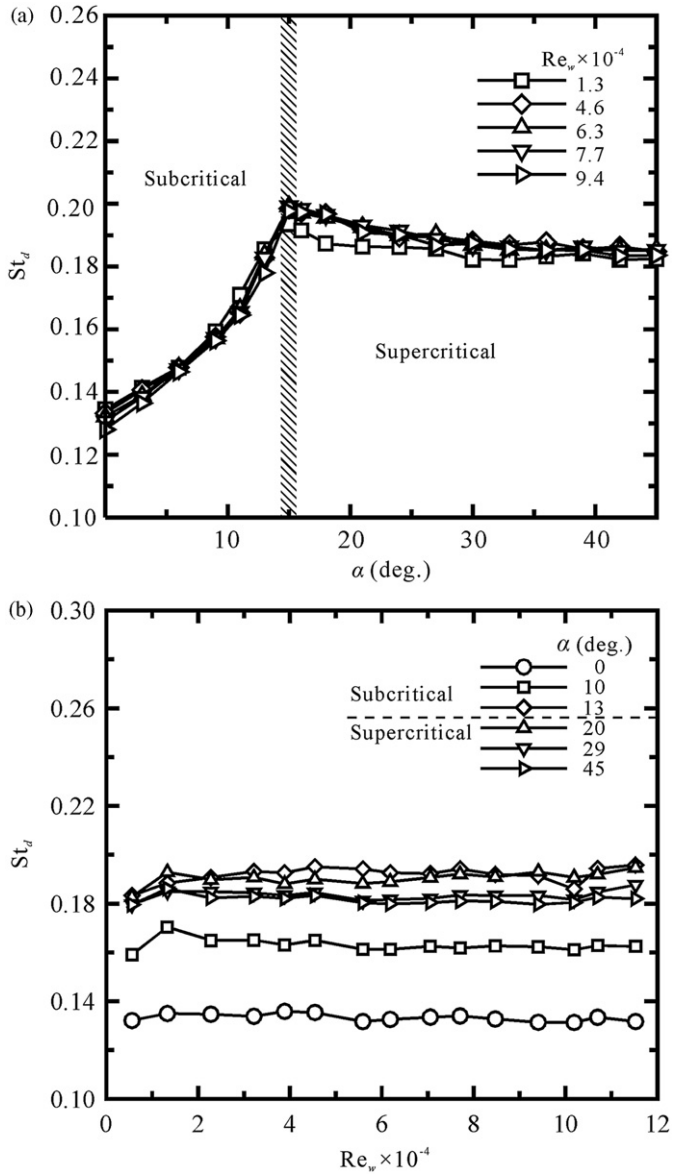

Fig. 12. Strouhal number based on projection width of cylinder on cross-stream plane: (a) variation with incidence angle, (b) variation with Reynolds number.

and gradually levels off to about 0.185 as α becomes greater than about 30–35°. At $\alpha = 45°$, the flow on faces A and B behaves like the wedge flow while on faces C and D behave like a tail-body extruded downstream into the wake. The existence of the tail-body in the wake might cause the Strouhal number to increase slightly from 0.18 for the 90° wedge flow without tail-body to 0.185 as obtained in this case. If the conventional figure for the Strouhal number/Reynolds number relationship is plotted, as shown in Fig. 12(b), the distributions look like most of the correlation curves which were reported for investigations on circular cylinders (Zdravkovich, 1997), airfoils (Lissaman, 1983), flat plates (Novak, 1973), etc. The Strouhal number increases with increasing Reynolds number in the low Reynolds number regime, attains a local maximum at a critical Reynolds number, then decreases a little and levels off in the high Reynolds number regime. However, the correlated Strouhal numbers disperse widely for different incidence angles although the width of the projection on the cross-stream plane instead of the cylinder width is used for calculation.

Roshko (1955) and Simmons (1977) introduced a "universal" Strouhal number St* based on the measured wake width d^* for several types of two-dimensional bluff bodies. They found that the universal Strouhal number St* for several different shapes of bluff bodies would present similar values of about 0.163. Roshko also applied, successfully, the inviscid Kirchhoff's free streamline theory to relate the drag to the universal Strouhal number by using a k function, which implied that the application of inviscid model to the bluff-body wake at large Reynolds numbers is appropriate. Levi (1983) justified Roshko and Simon's universal Strouhal law by modeling the available specific kinetic energy $U^2/2$ of the oscillating fluid by the specific mechanical energy $(2\pi f_s d^*)^2/2$ of the oscillator which oscillates at frequency f_s within the width d^*. The universal Strouhal number St* turned out to be $1/2\pi = 0.159$. The result of the energy model seemed to be very close to that of these specific experiments. As mentioned previously, in the present study the correlated Strouhal numbers shown in Fig. 12(b) disperse widely for different incidence angles. In order to examine the appropriateness of applying the "universal" Strouhal number to the case of square cylinder, the wake widths at various incidence angles are estimated by measuring the axial velocities in the near wake ($x/w = 1$, $z/w = 0$) along the cross-stream direction by using an single-wire hot wire anemometer. The results are discussed as follows.

The time-averaged axial velocity distributions along the cross-stream direction (which are not shown here) present deficit values in the wake of the square cylinder, and gradually increase to freestream values outside the wake region. It is therefore very difficult to identify the wake width according to the cross-stream distributions of the axial velocities. The cross-stream distributions of the turbulence intensities (as typically shown in Fig. 13(a) for $\mathrm{Re}_w = 7.7 \times 10^4$), however, present twin-peak patterns. The peak values on the turbulence-intensity distributions would appear at the inversion points on the cross-stream distributions of the time-averaged axial velocities, and are located in the shear layers (Brown and Roshko, 1974). Therefore, the distance between these two peaks could be used as an appropriate index for estimating the length scale of the wake width (Tennekes and Lumley, 1983). Fig. 13(b) shows the maximum values of the turbulence intensities in the shear layers at various Reynolds numbers. The maximum turbulence intensity T_{SL} increases with increasing the incidence angle in the subcritical regime, drops abruptly to attain a minimum value at the critical incidence angle $\alpha = 15°$, then increases with increasing incidence angle in the supercritical regime.

The normalized cross-stream coordinates $y_{SL,B}/w$ and $y_{SL,C}/w$ for the locations of the peak turbulence intensities are plotted with respect to the incidence angle and are shown in Fig. 14(a). At $\alpha = 0°$ and 45°, the locations where the two peak turbulence intensities appear are almost symmetric about $y = 0$. This is because the geometries of the square cylinder at $\alpha = 0°$ and 45° are symmetric about x-axis. With the increase of the incidence angle, the shear layer evolving from the leading edge of face C (indicated by $y_{SL,C}$) generally moves outwards (i.e., towards the $+y$ direction). This is because the separated boundary layer evolving from the junction between faces A and C never reattaches to face C as the junction between faces A and C moves outwards with increasing the incidence angle. At the critical incidence angle $\alpha = 15°$, the shear layer moves a little inwards because the flow pattern on face C changes from a dual-ring bubble located near the leading edge of face C to a wide, shallow bubble covering the rear surface of face C, as has been shown in Figs. 9(a) and (b). The shear layer evolving from the leading edge of face B (indicated by $y_{SL,B}$) moves inwards (i.e., towards the $+y$ direction) with the increase of α in the subcritical regime and *vice versa* in the supercritical regime. In the subcritical regime, since the junction between faces A and B moves inwards with increasing angle of attack, the separated boundary-layer does not reattach to the surface. At the critical incidence angle $\alpha = 15°$, the separated boundary-layer reattaches to face B. The boundary-layer separation occurs at the junction between faces B and D, and therefore makes the shear layer move drastically inwards. In the supercritical regime, the junction between face B and face D moves towards the -y direction with increasing incidence angle. Therefore, the boundary layer which separates from there turns out to be deflected outwards. The normalized length scale of the wake width, which is defined as $w'/w = y_{SL,C}/w - y_{SL,B}/w$, is shown in Fig. 14(b). The minimum wake width does not occur at $\alpha = 0°$ where the cross-stream width of the square cylinder has a minimum value w. The minimum length scale of the wake width ($w'/w = 1.08$) appears at the critical incidence angle $\alpha = 15°$. The maximum value ($w'/w = 1.67$) is present at $\alpha = 45°$. The normalized cross-stream projection of the square cylinder, d/w, is 1.23 and 1.41 at $\alpha = 15°$ and 45°, respectively. At $\alpha = 15°$, the normalized wake width is 12.2% smaller than the normalized projection width of the cylinder. At $\alpha = 45°$, w'/w is

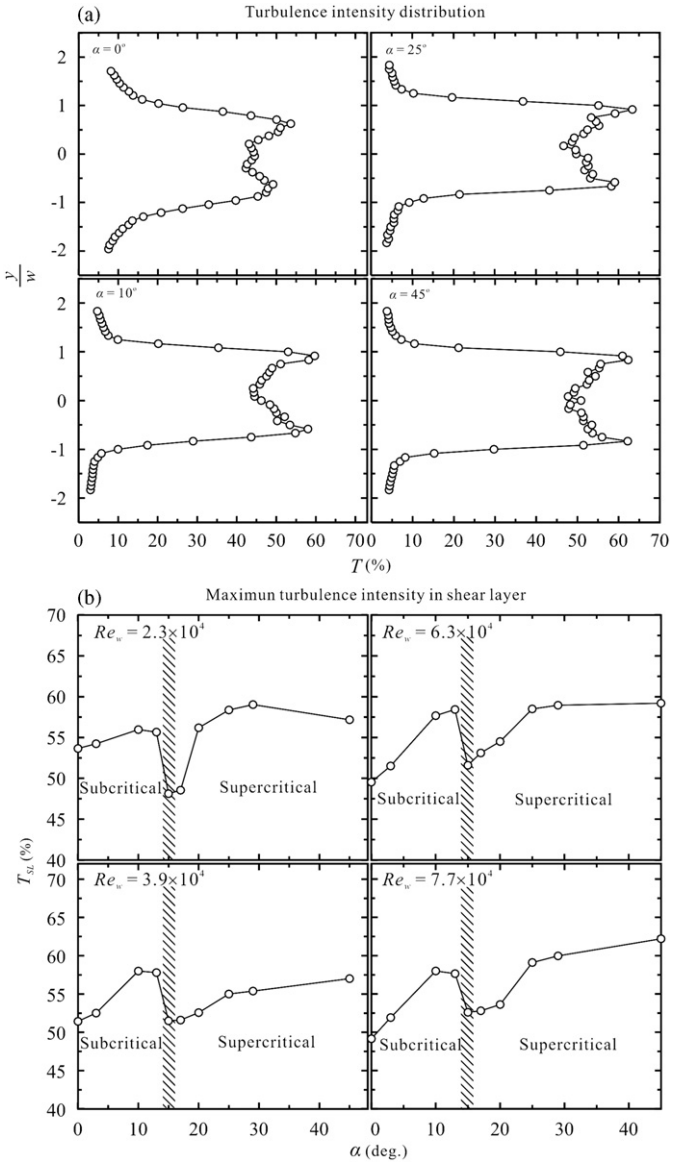

Fig. 13. Axial turbulence intensity near wake measured at ($x/w = 1$, $z/w = 0$). (a) Turbulence intensity distribution along cross-stream direction, $\mathrm{Re}_w = 7.7 \times 10^4$; (b) variation of maximum turbulence intensity (which appears in shear layer) with incidence angle.

35.8% larger than d/w. Apparently, the dramatic reduction of the wake width at the critical incidence angle is closely related to the change of the flow patterns on faces B and C in the subcritical and supercritical regimes. The reattachment of the separated boundary-layer on face B and the disappearance of the leading-edge bubble on face C as the incidence angle increases from the subcritical regime to the supercritical regime are the primary factors leading to this phenomenon. The wake width can affect the aerodynamic forces developed on the cylinder. As a side note, the surface pressures of the square cylinder at various incidence angles were measured by the authors, but are not presented in this paper. The lift and drag coefficients were obtained by integrating the surface pressures over the four faces. When the square cylinder rotates from 0° to 45° in a crossflow, it presents a minimum drag and a maximum lateral force at the critical incidence angle. The lift and drag coefficients measured by Obasaju (1983) and Lee (1975) display the same characteristics at the critical incidence angle as the results measured by the present authors.

Redefining a Strouhal number as $\mathrm{St}_{w'} \equiv fw'/U$ based on the length scale of the wake width w' instead of using the cross-stream projection w, the Strouhal number distributions can be categorized into two groups, as shown in Fig. 15. The

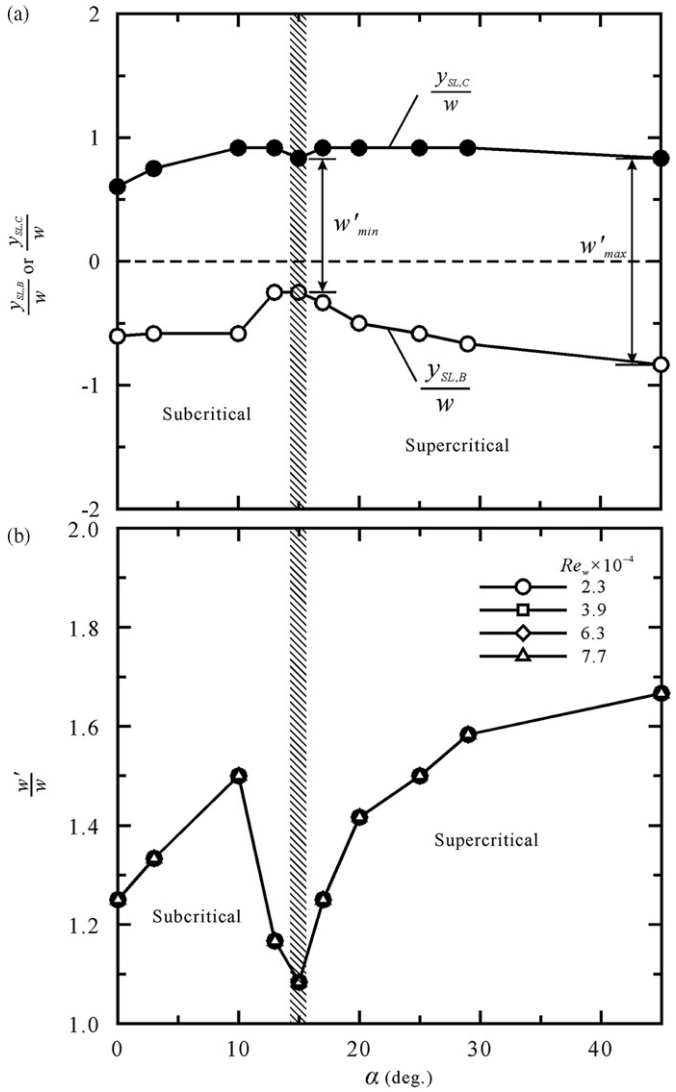

Fig. 14. Transverse length scale of wake width at $(x/w, z/w) = (1, 0)$. (a) Locations of peak turbulence intensities, $Re_w = 7.7 \times 10^4$; (b) wake width.

distributions of $St_{w'}$ in the subcritical regime are collapsed into a narrow band with smaller values. Those in the supercritical and wedge flow regimes fall into another narrow band with larger values of $St_{w'}$. All values of $St_{w'}$ approach constants as the Reynolds number becomes greater than about 2.3×10^4. The constants for the subcritical and supercritical regimes are approximately 0.172 and 0.214, respectively. The former is a little larger than the "universal" Strouhal number obtained by Roshko (1955) and Simons (1977), while the latter is quite similar to the values obtained by many investigators for the circular cylinder [e.g., Zdravkovich (1997)].

4. Summary and conclusions

Time-averaged topological flow patterns around a square cylinder in crossflow at incidence are proposed based on the experimental results of the surface-oil flow patterns. The flows around the square cylinder are identified as three categories: the *subcritical*, *supercritical*, and *wedge* flows according to the prominently different features of the topological flow patterns. In the subcritical regime ($0^\circ \leq \alpha < 15^\circ$), the boundary layers separate from the leading edges of

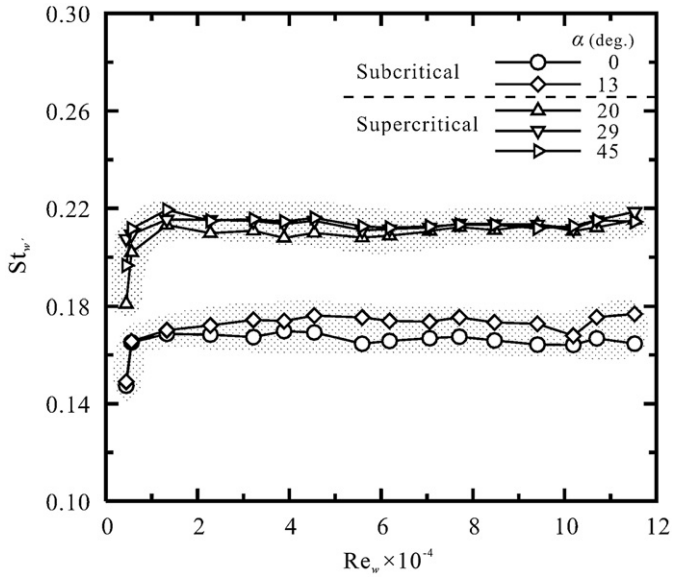

Fig. 15. Strouhal numbers calculated based on wake width measured at $(x/w, z/w) = (1, 0)$.

the lateral faces of the square cylinder and never reattach to the surfaces. In-between the separated boundary layers and the lateral faces, small dual-ring bubbles exist near the leading edges of the lateral faces. In the supercritical regime ($15^\circ \leq \alpha < 45^\circ$), the separated boundary layer on the lateral surface facing windward reattaches to the surface and hence forms a recirculation bubble. On the lateral surface facing leeward, the separated boundary layer never reattaches to the surface; instead, a shallow and wide recirculation bubble covering the rear part of the surface is formed. At incidence angle 45°, a symmetric wedge flow is observed on the two surfaces facing windward. The Strouhal number of vortex shedding, turbulence in the wake, and wake width present different characteristics in different characteristic flow regimes, and have close correlations with the flow patterns.

At the critical incidence angle 15°, which separates the subcritical and supercritical regimes, the Strouhal number of vortex shedding attains a maximum of 0.2, and the wake width presents a minimum value of $1.08w$. The change of the flow patterns on the lateral surfaces at the critical incidence angle reduce the wake width to a minimum, which contributes to a maximum Strouhal number and a minimum drag coefficient. If the Strouhal numbers of the vortex shedding are calculated based on the cross-stream projection width of the square cylinder, a wide dispersion of the data will be obtained for vortex shedding frequencies at various incidence angles. By taking the wake width as the length scale, the Strouhal numbers in the subcritical and supercritical regimes are well correlated into two groups which would approach constants of 0.172 and 0.214, respectively, at high Reynolds numbers.

References

Bearman, P.W., Trueman, D.M., 1972. An investigation of the flow around rectangular cylinders. Aeronautical Quarterly 23, 229–237.
Bejan, A., 1984. Convection Heat Transfer. John Wiley & Sons, New York, pp. 110–114.
Brown, G.L., Roshko, A., 1974. On density effects and large structures in turbulent mixing layers. Journal of Fluid Mechanics 64, 775–816.
Cheng, M., Whyte, D.S., Lou, J., 2007. Numerical simulation of flow around a square cylinder in uniform-shear flow. Journal of Fluids and Structures 23, 207–226.
Chong, M.S., Perry, A.E., 1990. A general classification of three-dimensional flow fields. Physics of Fluids A 2, 765–777.
Durão, D.F.G., Heitor, M.V., Pereira, J.C.F., 1988. Measurements of turbulent and periodic flows around a square cross-section cylinder. Experiments in Fluids 6, 298–304.
Dutta, S., Muralidhar, K., Panigrahi, P.K., 2003. Influence of the orientation of a square cylinder on the wake properties. Experiments in Fluids 34, 16–23.
Fox, T.A., West, G.S., 1990. On the use of end plates with circular cylinders. Experiments in Fluids 9, 237–239.
Flagan, R.C., Seinfeld, J.H., 1988. Fundamentals of Air Pollution Engineering. Prentice Hall, Englewood Cliffs, pp. 295-307.

Gerich, D., Eckelmann, H., 1982. Influence of end plates and free ends on the shedding frequency of circular cylinders. Journal of Fluid Mechanics 122, 109–121.
Hu, J.C., Zhou, Y., Dalton, C., 2006. Effects of the corner radius on the near wake of a square prism. Experiments in Fluids 40, 106–118.
Huang, R.F., Shy, W.W., Lin, S.W., Hsiao, F.-B., 1996. Influence of surface flow on aerodynamic loads of a cantilever wing. AIAA Journal 34, 527–532.
Huang, R.F., Lee, H.W., 2000. Turbulence effect on frequency characteristics of unsteady motions in wake of wing. AIAA Journal 38, 87–94.
Hunt, J.C.R., Abell, C.J., Peterka, J.A., Woo, H., 1978. Kinematic studies of the flows around free or surface-mounted obstacles: applying topology to flow visualization. Journal of Fluid Mechanics 86, 179–200.
Igarashi, T., 1984. Characteristics of the flow around a square prism. Bulletin of JSME 27, 1858–1865.
Kareem, A., Cermak, J.E., 1984. Pressure fluctuations on a square building model in boundary-layer flows. Journal of Wind Engineering and Industrial Aerodynamics 16, 17–41.
Knisely, C.W., 1990. Strouhal numbers of rectangular cylinders at incidence: a review and new data. Journal of Fluids and Structures 4, 371–393.
Kurtulus, D.F., Scarano, F., David, L., 2007. Unsteady aerodynamic forces estimation on a square cylinder by TR-PIV. Experiments in Fluids 42, 185–196.
Lee, B.E., 1975. The effect of turbulence on the surface pressure field of a square prism. Journal of Fluid Mechanics 69, 321–352.
Levi, E., 1983. A universal Strouhal law. ASCE Journal of Engineering Mechanics 109, 718–727.
Lissaman, P.B.S., 1983. Low Reynolds number airfoils. Annual Review of Fluid Mechanics 15, 223–239.
Luo, S.C., Tong, X.H., Khoo, B.C., 2007. Transition phenomena in the wake of a square cylinder. Journal of Fluids and Structures 23, 227–248.
Lyn, D.A., Einav, S., Rodi, W., Park, J.-H., 1995. A laser-Doppler velocimetry study of ensemble-averaged characteristics of the turbulent near wake of a square cylinder. Journal of Fluid Mechanics 304, 285–319.
Lyn, D.A., Rodi, W., 1994. The flapping shear layer formed by separation from the forward corner of a square cylinder. Journal of Fluid Mechanics 267, 353–376.
Merzkirch, W., 1974. Flow Visualization. Academic Press, New York, pp. 53–66.
Mueller, T.J., 1983. Flow visualization by direct injection. In: Goldstein, R.J. (Ed.), Fluid Mechanics Measurements. Hemisphere Publishing, New York, pp. 307–340.
Norberg, C., 1993. Flow around rectangular cylinders: pressure forces and wake frequencies. Journal of Wind Engineering and Industrial Aerodynamics 49, 187–196.
Novak, J., 1973. Strouhal number and flat plate oscillation in an air stream. Acta Technica CASV 4, 372–386.
Obasaju, E.D., 1983. An investigation of the effects of incidence on the flow around a square section cylinder. Aeronautical Quarterly 34, 243–259.
Okajima, A., 1982. Strouhal numbers of rectangular cylinders. Journal of Fluid Mechanics 123, 379–398.
Ozgoren, M., 2006. Flow structure in the downstream of square and circular cylinders. Flow Measurement and Instrumentation 17, 225–235.
Perry, A.E., Fairlie, B.D., 1974. Critical points in flow patterns. Advances in Geophysics 18, 299–315.
Perry, A.E., Steiner, B.D., 1987. Large-scale vortex structures in turbulent wakes behind bluff bodies. Part I. Vortex formation. Journal of Fluid Mechanics 174, 233–270.
Rockwell, D.O., 1977. Organized fluctuations due to flow past a square cross section cylinder. ASME Journal of Fluids Engineering 99.
Roshko, A., 1955. On the wake and drag of bluff bodies. Journal of Aerospace Sciences 22, 124–235.
Saha, A.K., Muralidhar, K., Biswas, G., 2000. Experimental study of flow past a square cylinder at high Reynolds numbers. Experiments in Fluids 29, 553–563.
Saha, A.K., Muralidhar, K., Biswas, G., 2000. Vortex structure and kinetic energy budget in two-dimensional flow past a square cylinder. Computers & Fluids 29, 669–694.
Sarioglu, M., Akansu, Y.E., Yavuz, T., 2005. Control of flow around square cylinders at incidence by using a rod. AIAA Journal 43, 1419–1426.
Simmons, J.E.L., 1977. Similarities between two-dimensional and axisymmetric vortex wakes. Aeronautical Quarterly 28, 15–20.
Squire, L.C., 1961. The motion of a thin oil sheet under the steady boundary layer on a body. Journal of Fluid Mechanics 11, 161–179.
Stansby, P.K., 1974. The effects of end plates on the base pressure coefficient of a circular cylinder. Aeronautical Journal 78, 36–37.
Strouhal, V., 1878. Über eine besondere Art der Tonerregung. Annalen der Physik und Chemie, Neue Folge, Heft, October, pp. 216–251.
Szepessy, S., Bearman, P.W., 1992. Aspect ratio and end plate effects on vortex shedding from a circular cylinder. Journal of Fluid Mechanics 234, 191–217.
Tennekes, H., Lumley, J., 1983. A First Course in Turbulence. The MIT Press, New York.
Tong, X.H., Luo, S.C., Khoo, B.C., 2008. Transition phenomena in the wake of an inclined square cylinder. Journal of Fluids and Structures 24, 994–1005.
Tamura, T., Miyagi, T., 1999. The effect of turbulence on aerodynamic forces on a square cylinder with various corner shapes. Journal of Wind Engineering and Industrial Aerodynamics 83, 135–145.

Taylor, I., Vezza, M., 1999. Prediction of unsteady flow around square and rectangular section cylinders using a discrete vortex method. Journal of Wind Engineering and Industrial Aerodynamics 82, 247–269.

Vickery, B.J., 1966. Fluctuating lift and drag on a long cylinder of square cross-section in a smooth and in a turbulent stream. Journal of Fluid Mechanics 25, 481–494.

van Oudheusden, B.W., Scarano, F., van Hinsberg, N.P., Watt, D.W., 2005. Phase-resolved characterization of vortex shedding in the near wake of a square-section cylinder at incidence. Experiments in Fluids 39, 86–98.

West, G.S., Apelt, C.J., 1982. The effects of tunnel blockage and aspect ratio on the mean flow past a circular cylinder with Reynolds number between 10^4 and 10^5. Journal of Fluid Mechanics 114, 361–377.

Zdravkovich, M.M., 1997. Flow around Circular Cylinders. Oxford University Press, Oxford, UK.